PHOTONICS Research

Photonic-reconfigurable entanglement distribution network based on silicon quantum photonics

Dongning Liu,[1] Jingyuan Liu,[1] Xiaosong Ren,[1] Xue Feng,[1] Fang Liu,[1] Kaiyu Cui,[1] Yidong Huang,[1,2] and Wei Zhang[1,2,*]

[1]Frontier Science Center for Quantum Information, Beijing National Research Center for Information Science and Technology (BNRist), Electronic Engineering Department, Tsinghua University, Beijing 100084, China
[2]Beijing Academy of Quantum Information Sciences, Beijing 100193, China
*Corresponding author: zwei@tsinghua.edu.cn

Received 3 March 2023; revised 29 April 2023; accepted 5 May 2023; posted 9 May 2023 (Doc. ID 489139); published 28 June 2023

The entanglement distribution network connects remote users by sharing entanglement resources, which is essential for realizing quantum internet. We propose a photonic-reconfigurable entanglement distribution network (PR-EDN) based on a silicon quantum photonic chip. The entanglement resources are generated by a quantum light source array based on spontaneous four-wave mixing in silicon waveguides and distributed to different users through time-reversed Hong–Ou–Mandel interference by on-chip Mach–Zehnder interferometers with thermo-optic phase shifters (TOPSs). A chip sample is designed and fabricated, supporting a PR-EDN with 3 subnets and 24 users. The network topology of the PR-EDN could be reconfigured in three network states by controlling the quantum interference through the TOPSs, which is demonstrated experimentally. Furthermore, a reconfigurable entanglement-based quantum key distribution network is realized as an application of the PR-EDN. The reconfigurable network topology makes the PR-EDN suitable for future quantum networks requiring complicated network control and management. Moreover, it is also shown that silicon quantum photonic chips have great potential for large-scale PR-EDN, thanks to their capacities for generating and manipulating plenty of entanglement resources.

https://doi.org/10.1364/PRJ.489139

1. INTRODUCTION

Quantum entanglement is the crucial resource of quantum information, which is the basis of many important applications of quantum communication and quantum information processing. An entanglement distribution network (EDN) distributes quantum entanglement resources to different parties, which is an essential step in the development of quantum internet [1,2], by which quantum information is shared and transported. Several repeater-free long-distance point-to-point entanglement distribution experiments have already been reported, such as the experiments over 300 km in fiber [3], 144 km in free space [4], and 1200 km from satellite to ground [5]. In these works, the quantum entanglement is carried by entangled photon pairs, which could be generated by the spontaneous parametric down-conversion (SPDC) in χ^2 nonlinear media such as nonlinear crystals [6,7] and periodically poled nonlinear waveguides [8–13], and spontaneous four-wave mixing (SFWM) in χ^3 nonlinear media, such as silica optical fibers [14–17] and silicon waveguides [18–21]. Since both processes support broadband entangled photon pair generation, multiple entanglement resources could be selected by wavelength-division multiplexing (WDM) to connect different users. In this way, EDNs with star-type layouts could realize a fully connected network with a mesh topology [22–32]. However, the user number of the EDN based on WDM would be limited by the spectrum of entangled photon pairs and bandwidth of the low-loss transmission window of optical fibers. It is a barrier to realizing large-scale quantum networks by WDM.

One way to break this barrier is realizing EDN based on both space-division multiplexing (SDM) and WDM. It has been investigated in several works [26,27,30] of entanglement-based quantum key distribution (QKD) networks. The entanglement resources generated by a quantum light source are divided by WDM. They could be used to support subnets through passive multi-port beam splitters. They could also be used to realize the interconnection between users in different subnets. In this way, a fully connected QKD network with 40 users has been achieved by only one SFWM quantum light source [30]. However, the user number of this EDN is still limited by the total entanglement resources provided by the quantum light source. Besides, the port number of the passive beam splitter is also limited by the loss due to its splitting ratio.

Moreover, since both WDM- and SDM-based EDNs consist of only passive components, they are static networks in which the distribution of entanglement resources could not be controlled on demand. Hence, it is difficult to apply them in the scenarios requiring network control and management.

In recent years, silicon quantum photonics has developed rapidly. Single mode silicon waveguides and silicon micro-ring resonators are ideal χ^3 nonlinear media to realize quantum light sources for entangled photon pair generation. The fabrication of silicon photonic chips is compatible with complementary metal–oxide–semiconductor (CMOS) technology, which provides the ability to realize a large-scale quantum photonic circuit in a finger-sized area. Various quantum photonic functions have been realized by silicon quantum photonic chips, including entanglement states generation in different degrees of freedom [33–36], quantum communication [37–44], and quantum computation [45–48]. In these works, complicated photonic quantum states are realized by arrays of SFWM quantum light sources and are manipulated by arrays of optical interferometers, achieving sophisticated quantum information functions. It is natural to utilize the established silicon quantum photonic functionalities to improve the scale and the capability of EDNs. The array of quantum light sources on the silicon photonic chip could provide rich quantum entanglement resources to support a large-scale EDN. Moreover, the quantum state manipulation on the chip could support the controllable quantum entanglement distribution for network reconfiguration.

In this work, we propose a photonic-reconfigurable entanglement distribution network (PR-EDN) based on a silicon quantum photonic chip. The entanglement resources of the PR-EDN are generated by an array of SFWM quantum light sources and distributed to users by the controllable SDM on the chip, which is realized by on-chip quantum interference. In the experiment, we design and fabricate a chip on a silicon-on-insulator (SOI) substrate with a 220 nm top-silicon layer, which supports a PR-EDN with 3 subnets and 24 users. The network topology is controlled in three states by thermal phase shifters on the chip. The performance of quantum entanglement distribution at different network topologies is measured experimentally, and their QKD applications are demonstrated, showing its potential for future quantum networks requiring complicated network control and management.

2. RESULTS

A. PR-EDN Based on the Silicon Quantum Photonic Chip

The entanglement resources required by the PR-EDN are generated by an array of SFWM quantum light sources on the silicon chip. The entangled photon pairs with specific signal/idler wavelengths are used to support the PR-EDN, which could be post-selected by optical filters at the user ends. This scheme fully utilizes the advantage of silicon photonics on the large-scale photonic integration and avoids complicated multi-wavelength multiplexing and demultiplexing on the chip. Moreover, since the effective entangled photon pairs generated by all the quantum light sources have the same joint spectral amplitude, these entanglement resources could be manipulated and distributed through quantum interference by on-chip interferometers. If the PR-EDN is applied as a QKD network, SDM by passive beam splitting could be applied to further extend the scale of the network. In such a QKD network, some entanglement resources are used to support fully connected subnets, and the rest of the entanglement resources are used to connect the users in different subnets. Hence, it can be expected that the network topology among the subnets could be controlled by the on-chip quantum interference, achieving the function of network reconfiguration.

Here, we design a silicon quantum photonic chip to demonstrate the main idea of this PR-EDN. It is fabricated on an SOI substrate with a 220 nm top-silicon layer. The propagation of lights/photons in the chip is realized by the fundamental quasi-TE mode of the silicon waveguide. The sketch of the chip design is shown in Fig. 1(a), and the microscope photograph of the fabricated chip sample is shown in Fig. 1(b). The entangled photon pairs are generated by SFWM in six long silicon waveguides (6.5 mm) on the chip. They are located in three balanced Mach–Zehnder interferometers (MZIs), which are named as biphoton state generation units (BSGUs). Besides the long waveguides, each BSGU has two 2 × 2 multimode interference (MMI) couplers and one thermo-optic phase shifter (TOPSs) on one arm of the MZI. The BSGUs are pumped by a mono-color continuous-wave (CW) pump light to generate energy-time entangled photon pairs. In each BSGU, the pump light is split into two parts coherently in the first MMI coupler. Then, they propagate along the waveguides in two arms and generate photon pairs by SFWM, which can be regarded as entangled states in the path degree of freedom. The biphoton state before the second MMI coupler is denoted by $|\Psi_1\rangle$, which is in the form of

$$|\Psi_1\rangle = \frac{1}{\sqrt{2}}(|1_s1_i\rangle_{\text{up}} + e^{i2\phi}|1_s1_i\rangle_{\text{down}}). \quad (1)$$

Here, $|1_s1_i\rangle_{\text{up}}$ ($|1_s1_i\rangle_{\text{down}}$) represents the state that a photon pair is generated in the up-arm (down-arm) of the MZI. The relative phase ϕ in $|\Psi_1\rangle$ can be controlled by the TOPS in the MZI. According to the process of time-reversed Hong–Ou–Mandel (HOM) interference [14,21], $|\Psi_1\rangle$ interferes in the second MMI coupler. The output state of the BSGU after the interference is denoted by $|\Psi_2\rangle$, which is related to the relative phase ϕ,

$$|\Psi_2\rangle = \cos\phi|\Psi_{\text{bunch}}\rangle + \sin\phi|\Psi_{\text{split}}\rangle, \quad (2)$$

$$|\Psi_{\text{bunch}}\rangle = \frac{1}{\sqrt{2}}(|1_s1_i\rangle_{\text{up}}|0_s0_i\rangle_{\text{down}} - |0_s0_i\rangle_{\text{up}}|1_s1_i\rangle_{\text{down}}), \quad (3)$$

$$|\Psi_{\text{split}}\rangle = \frac{1}{\sqrt{2}}(|1_s0_i\rangle_{\text{up}}|0_s1_i\rangle_{\text{down}} + |0_s1_i\rangle_{\text{up}}|1_s0_i\rangle_{\text{down}}). \quad (4)$$

In the state of $|\Psi_{\text{bunch}}\rangle$, the signal and idler photons in a pair would be output from the same output port of the BSGU, while which port they would be output from is random. In contrast, in the state of $|\Psi_{\text{split}}\rangle$, the signal and idler photons in a pair would be output from the two output ports of the BSGU, respectively. It is worth noting that these operations are in path degree of freedom and the output photon pairs still

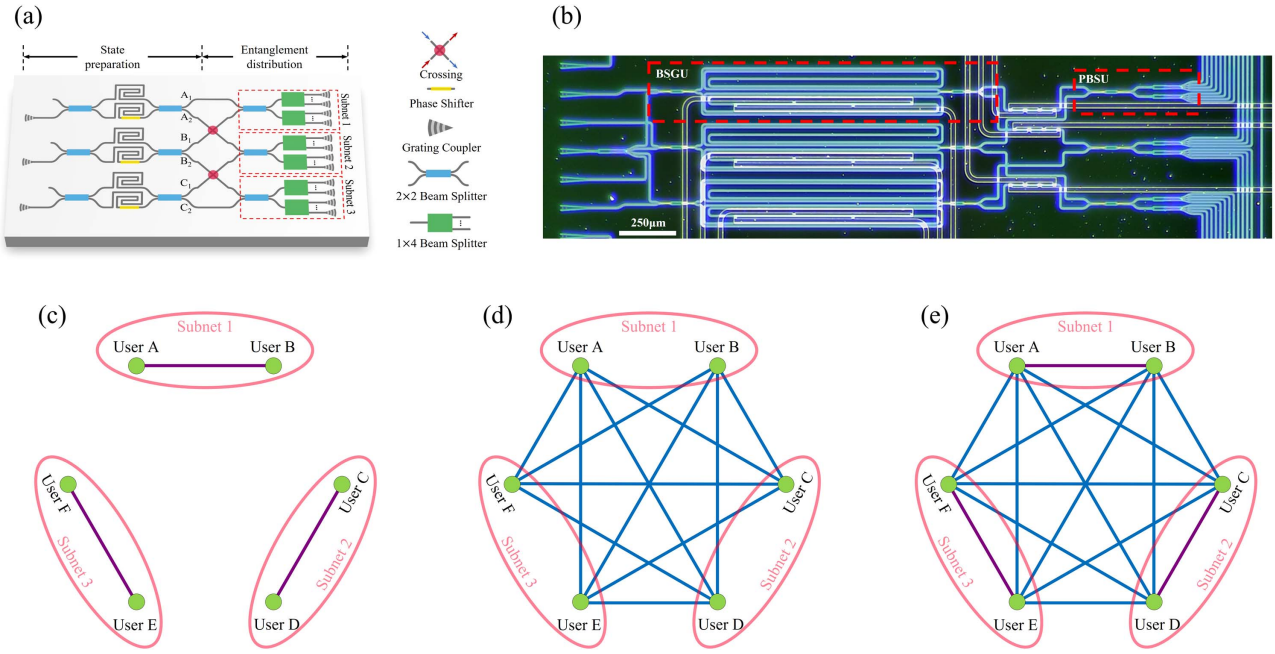

Fig. 1. Chip and the network topology. (a) Design of the silicon quantum photonic chip for the PR-EDN. The entangled photon pairs are generated in six long silicon waveguides by SFWM and distributed to different users by quantum interference and passive beam splitting. (b) Microscope photograph of the fabricated chip sample. The chip supports a PR-EDN with three subnets, which are denoted by Subnets 1, 2 and 3, respectively. Each subnet has eight users. We choose two users in each subnet to show the states of network topology at different configurations, which are denoted by (c) intra-subnet state, (d) inter-subnet state, and (e) all-subnet state.

have the property of energy-time entanglement, which is the entanglement resources provided by the chip.

The chip has three BSGUs. Their output ports are connected to three passive beam splitting units (PBSUs), as shown in Fig. 1(a). Two waveguide crossings are used to realize the connection between BSGUs and PBSUs. Each PBSU has one 2×2 MMI coupler and two 1×4 MMI beam splitters. As a result, it supports a subnet with eight users. Entanglement resources from different BSGUs are mixed up in the 2×2 MMI coupler to erase their information of paths. Then, the signal and idler photons are randomly distributed to eight output grating couplers by two 1×4 MMI beam splitters. The photons would be coupled into optical fibers through these grating couplers and sent to end users in the subnet. For two specific end users, the photon pairs they shared are post-selected according to their paths. They are at the energy-time entangled state, which supports applications such as QKD. As a result, the chip could support a PR-EDN of 24 users with 3 subnets.

It is shown in Fig. 1(a) that the pump lights are injected into three BSGUs through three independent grating couplers on the chip. If the pump lights in the three BSGUs are incoherent with each other, the quantum interference in the 2×2 MMI couplers of three PBSUs would be avoided. When the output states of the three BSGUs are all $|\Psi_2\rangle = |\Psi_{\text{bunch}}\rangle$ under $\phi = 0$, the signal and idler photons in a pair would be randomly distributed to two users in the same subnet. But the users in different subnets could not share entanglement resources. In this case, the network is at the intra-subnet state, and its network topology is shown in Fig. 1(c). When the output states of the three BSGUs are all $|\Psi_2\rangle = |\Psi_{\text{split}}\rangle$ under $\phi = \pi/2$, the signal and idler photons in a pair would be distributed to different subnets, establishing entanglement links between these subnets. However, the users in the same subnet could not share entanglement resources. In this case, the network is at the inter-subnet state, and its network topology is shown in Fig. 1(d). If the output states of the three BSGUs are the superposition of $|\Psi_{\text{split}}\rangle$ and $|\Psi_{\text{bunch}}\rangle$, any two users in the network could share entanglement resources with each other. It has a fully connected topology shown in Fig. 1(e), which is named as the all-subnet state. Consequently, the network topology of the PR-EDN can be reconfigured among the intra-subnet state, the inter-subnet state, and the all-subnet state by controlling the TOPSs in the three BSGUs.

B. Experimental Setup

The sketch of the experimental setup is shown in Fig. 2(a). The CW pump light is generated by a tunable laser (N7714A, Keysight Inc.) with a built-in function of frequency modulation. Its center wavelength is 1552.52 nm, corresponding to the International Telecommunication Union (ITU) channel of C31. A 500 MHz frequency modulation is applied to the pump light to reduce its coherent length to about 1 m. The pump light is amplified by an erbium-doped optical fiber amplifier (EDFA). The amplified spontaneous emission (ASE) of the EDFA is blocked by cascaded dense wavelength-division multiplexing (DWDM) components with an extinction ratio higher than 100 dB. Then, the pump light is divided equally into four paths by a 1×4 fiber beam splitter. One is used for power monitoring, and the other three are injected into the silicon quantum photonic chip through three grating couplers, pumping three BSGUs to generate entangled photon pairs. It is

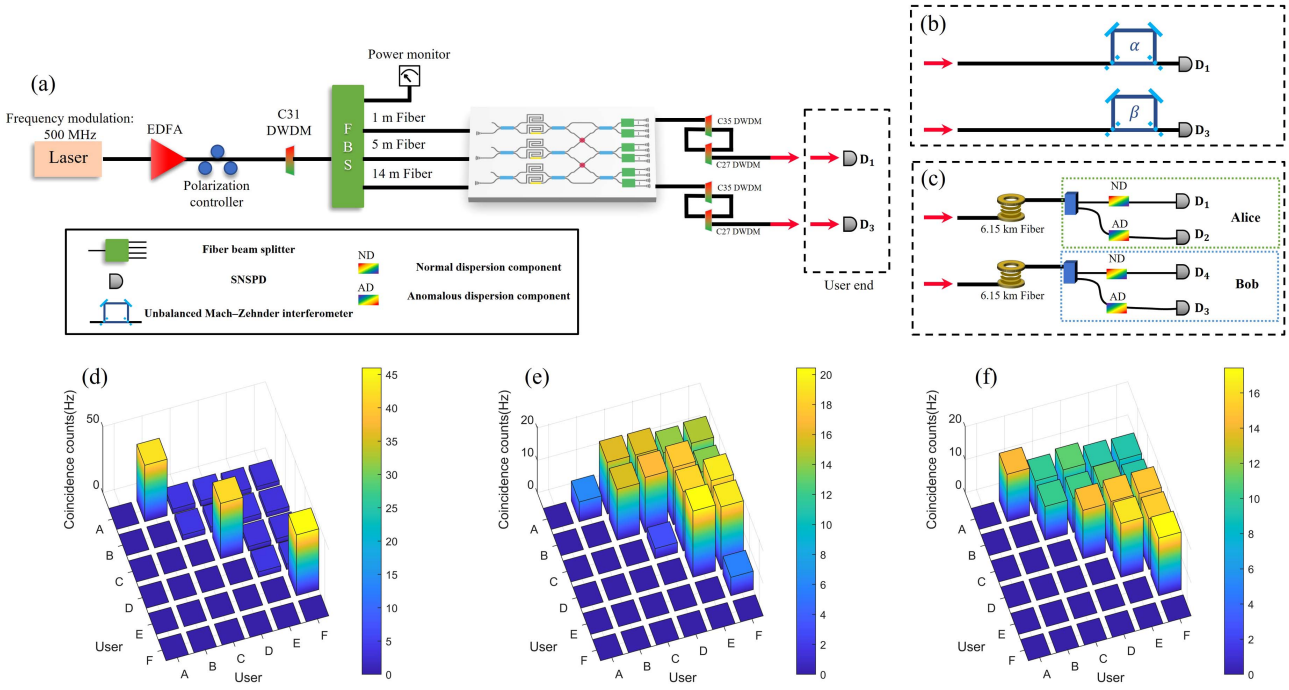

Fig. 2. Experimental setup and the results of entanglement distribution. (a) Experimental setup for the PR-EDN based on a silicon quantum photonic chip. In the experiment, we select two representative users from each subnet to demonstrate the characteristics of PR-EDN. They are users A and B of Subnet 1, users C and D of Subnet 2, and users E and F of Subnet 3. (b) Setup at user ends for Franson-type interference. (c) Setup at user ends for symmetric entanglement-based DO-QKD. (d)–(f) Results of coincidence counting between selected users at (d) intra-subnet state, (e) inter-subnet state, and (f) all-subnet state.

worth noting that the fiber lengths of the three paths (between the 1 × 4 fiber beam splitter and the silicon chip) are different, which are 1 m, 5 m, and 14 m, respectively. The length differences of these fibers are far larger than the coherent length of the pump light, ensuring that the biphoton states generated from the three BSGUs are incoherent with each other. According to the physical process of SFWM, the signal and idler photons are generated symmetrically around the center wavelength of the pump light (C31). A double-bandpass filter module consisting of DWDMs of C27 and C35 is used to post-select the signal and idler photons and remove the residual pump light after the generated photons outputted from the chip. Finally, the post-selected photons are detected by NbN superconducting nanowire single-photon detectors (SNSPDs) to demonstrate the entanglement distribution by coincidence counting. The dark counts of the SNSPDs used in our experiments are about 100 Hz. The network topology is manipulated by the TOPSs in the three BSGUs, which are controlled by a multi-channel digital-to-analog converter (DAC).

C. Reconfigurable Entanglement Distribution of the Network

To demonstrate the reconfigurable entanglement distribution of the network shown in Figs. 1(c)–1(e), we select two representative users from each subnet and measure the coincidence counts between them in the experiment. They are users A and B of Subnet 1, users C and D of Subnet 2, and users E and F of Subnet 3. The temporal width of coincidence window is 320 ps. The experimental results of the intra-subnet state are shown in Fig. 2(d). Only the users in the same subnet (AB, CD, and EF) have coincidence counts, showing that the entangled photon pairs can only be shared with the users in the same subnet at the intra-subnet state. In contrast, only the users in different subnets share the entangled photon pairs at the inter-subnet state. The experimental results are shown in Fig. 2(e). It is obvious that the coincidence counts between users in different subnets are much higher than those in the same subnet. The coincidence counts in the same subnet are mainly due to the calibration error of BSGUs, which could be avoided by more concise control of the thermal phase shifters in BSGUs. Figure 2(f) shows the results of the all-subnet state, showing that at this state a fully connected topology is achieved in this network with 24 users. The difference in the coincidence counts at three network states indicates that we can control the topology of this EDN through the TOPSs on the chip.

It is worth noting that the average coincidence count rates of the intra-subnet state, inter-subnet state, and all-subnet state are 43.5 Hz, 16.9 Hz, and 12.6 Hz, respectively. The difference of these measured rates is due to the different number of links sharing the entangled photon pairs at the three network states. The quantity of the entangled photon pairs provided by the chip is constant when the network topology changes by controlling the TOPSs. It can be expected that the average coincidence count rate would be higher if the network state has fewer links. In this PR-EDN, the numbers of links at the intra-subnet state, the inter-subnet state, and the all-subnet state are 84, 192, and 276, respectively. Hence, the intra-subnet state has the highest average coincidence count rate, while the all-state state has the lowest one. It shows that the PR-EDN could not

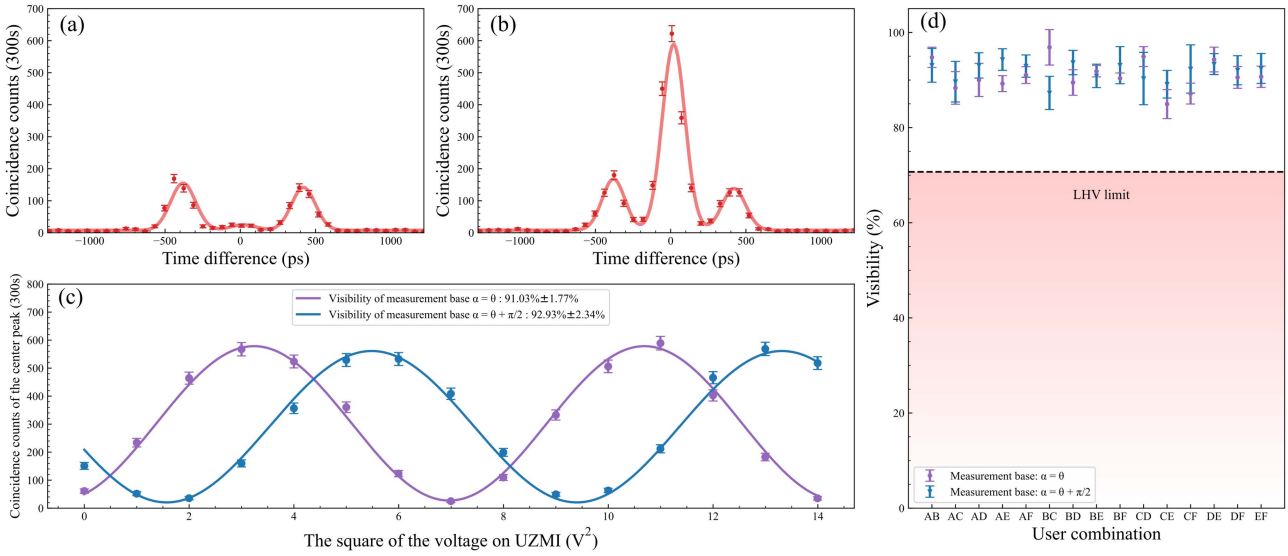

Fig. 3. Experimental results of Franson-type interference. Typical results of time-resolved coincidence counting in the experiment of Franson-type interference on the link between users A and F, when the center peak of coincidence counts reaches its (a) minimum and (b) maximum. (c) Two-photon interference fringes measured in the experiment of Franson-type interference on the link between users A and F. The blue and purple points are experimental data measured under two mutually unbiased bases, respectively. We perform coincidence measurements for 300 s for each data point. Error bars come from the Poisson distribution of photons. The blue and purple lines are their fitting curves. Here, β is represented by the squares of the voltages on the corresponding UMZIs. (d) Raw visibilities of the Franson-type interference on all the 15 links among users A–F. All of them are higher than the local hidden variable (LHV) limit (70.7%).

only change the network topology but could also adjust the quantity of entangled photon pairs shared by specific links. It would improve the flexibility of quantum networks significantly.

Then, the experiments of Franson-type interference are implemented to verify the energy-time entanglement carried by the photon pairs [49], which are the entanglement resources distributed by the PR-EDN. In the experiments, the signal and idler photons sent to two users are passed through two unbalanced Mach-Zehnder interferometers (UMZIs) and then detected, respectively, as shown in Fig. 2(b). Each UMZI has a resistive heater to control the phase difference between its two arms. The phase differences of the two UMZIs are denoted by α and β, respectively. The time-resolved coincidence counting measurement of the Franson-type interference would have three coincidence peaks. The first (third) peak is contributed by the coincidences that the signal photon passes through the long (short) arm in one UMZI and the idler photon passes through the short (long) arm in another UMZI. The center peak is contributed by the coincidences that the signal and idler photons both pass through the long arms in the two UMZIs or they both pass through the short arms in the two UMZIs, which are indistinguishable and lead to a two-photon interference [49]. Coincidence counts of the center peak would vary sinusoidally when the total phase differences of the two UMZIs ($\phi = \alpha + \beta$) vary, showing a two-photon interference fringe. If the fringe visibilities are higher than $1/\sqrt{2}$ (70.7%) under two mutually unbiased bases (i.e., $\alpha = \theta$ and $\alpha = \theta + \pi/2$, where θ could be any value), it shows the violation of Bell's inequality [50,51], which verifies that the measured photon pairs have the property of energy-time entanglement.

In the experiments, the topology of the PR-EDN is set at the all-subnet state without loss of generality. The Franson-type interference is measured on all the links among the six selected users (users A–F). For each measurement, the time-resolved coincidence counts are recorded under different β when α is fixed at $\alpha = \theta$ and $\alpha = \theta + \pi/2$, respectively. The typical experiment results of the link between users A and F are shown in Figs. 3(a)–3(c). Figures 3(a) and 3(b) show the typical results of time-resolved coincidence counts when the center peak of coincidence counts reaches its minimum [Fig. 3(a)] and maximum [Fig. 3(b)], respectively. The coincidence counts of the center peaks at different β are shown in Fig. 3(c), which are the fringes of two-photon interference. The blue and purple points are the experimental data measured under $\alpha = \theta$ and $\alpha = \theta + \pi/2$, respectively. Since the phase differences of the UMZIs are proportional to squares of the voltages applied on the heaters of the two UMZIs, β is represented by the squares of the voltages on the corresponding UMZIs. It can be seen that sinusoidal interference fringes under two mutually unbiased bases can be obtained clearly. The raw visibilities (without subtracting accidental coincidence counts) of the two fringes are $91.03\% \pm 1.77\%$ and $92.93\% \pm 2.34\%$, respectively, showing the violation of Bell's inequality. The raw visibilities of the Franson-type interference on all the 15 links among users A–F are summarized in Fig. 3(d). The raw visibilities of all the measured fringes are higher than 84%. It shows that the PR-EDN chip can distribute high-quality energy-time entanglement to different users, no matter if the two users are in the same subnet or in different subnets. (The detailed experimental results of the Franson-type interference are shown in Appendix D.)

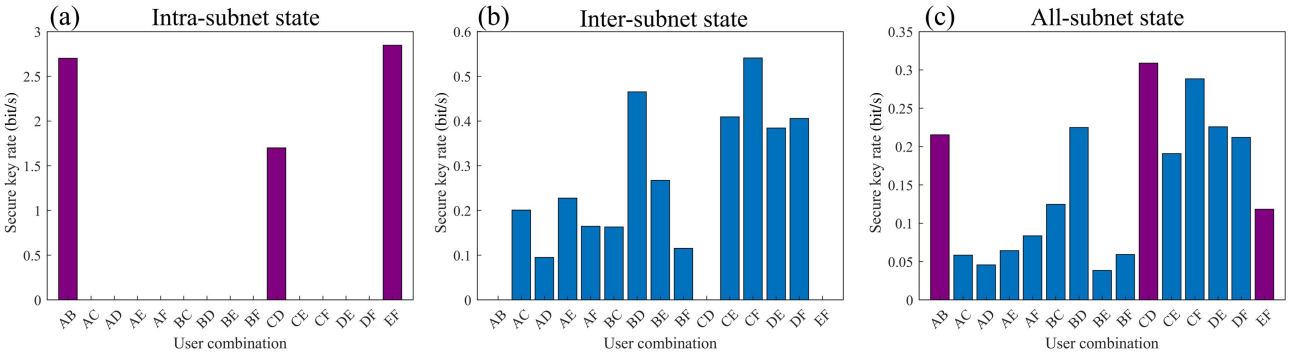

Fig. 4. Experimental results of the reconfigurable QKD network. Secure key rates of all the 15 links among the six users (users A–F) of the network at the (a) intra-subnet state, (b) inter-subnet state, and (c) all-subnet state. The secure keys are generated by the symmetric entanglement-based DO-QKD.

D. Reconfigurable QKD Network Based on the PR-EDN

The proposed PR-EDN could be used to realize a reconfigurable QKD network. We demonstrate this application by symmetric entanglement-based dispersion optics QKD (DO-QKD) [26] utilizing the resources of energy-time entanglement shared by the links in the network. In this experiment, the post-selected photons are not detected directly but are transmitted to QKD users (Alice and Bob) by optical fibers of 6.15 km, as shown Fig. 2(c). The photons received by Alice (or Bob) are split into two paths by a 50:50 fiber coupler. In each path, the photons pass through a dispersion component and are then detected by an SNSPD. The dispersion values of the two dispersion components in the two paths have the same magnitude but opposite sign, supporting the symmetric entanglement-based DO-QKD in the network. In the experiment, we measure the QKD performance of all the 15 links among the six users (users A–F) at three network states. Each link has a fiber transmission of 12.3 km. The measurement time of each link is several hours, ensuring that the impact of finite-size effect could be considered. The details of the key generation and security test are introduced in Appendix C.

The experimental results of the QKD network at the three states are shown in Fig. 4. The secure key rates (after the bin sifting and considering the performance of error correction and private amplification [52]) of all the network links at the intra-subnet state are shown in Fig. 4(a). It can be seen that only three links of AB, CD, and EF generate secure keys by the QKD process. Other links between two different subnets do not support QKD. It is because only the two users in the same subnet share entanglement resources at this state. In contrast, as shown by the measured secure key rates of the links at the inter-subnet state, only the links between two different subnets could generate secure keys by QKD, while the links of the two users in the same subnet do not support QKD. When the network is adjusted to the all-subnet state, since all the links could share entanglement resources, the secure keys are generated by QKD in all the links, as shown in Fig. 4(c). The intra-subnet state has the highest average secure key rate, while the all-subnet state has the lowest one among three states. This is due to the difference in the number of links sharing the entanglement resources. Details of the QKD performance measurement, including the raw key rates and the quantum bit error rate (QBER), are introduced in Appendix C. These experimental results show that the topology of this QKD network can be reconfigured by controlling the TOPSs on the chip.

3. DISCUSSION

A. Performance of the QKD Network

In the experiment, the average secure key rates are 1.98, 0.53, and 0.32 bit/s for the networks at the intra-subnet state, inter-subnet state, and all-subnet state, respectively. The low secure key rates are partly due to the loss of the experiment system. The loss of each link in the QKD networks can be divided into the on-chip loss and the off-chip loss. The on-chip loss is mainly from the coupling loss between the chip and optical fibers through the on-chip grating couplers. In this chip sample, the center wavelength of the grating couplers is shifted to 1580 nm due to the process variation in the fabrication (see Appendix B for more details). As a result, the coupling loss at the signal/idler wavelengths is about 6 dB. It could be reduced to less than 1 dB if more complicated mode size converters and coupling methods developed in recent years are used [53–55]. In a network link, two grating couplers are required for distributing photons to two different users. Therefore, an improvement of 10 dB could be expected on the coincidence count rate by improving the coupling between the chip and optical fibers, leading to a much better performance of QKD. The off-chip loss includes the contributions of optical fibers (12.3 km, ∼2.5 dB), double-bandpass filter module consisting of cascaded DWDMs for signal/idler photons (∼2 dB × 2), 50:50 fiber couplers (3 dB × 2), dispersion components (∼3 dB × 2) and efficiencies of SNSPDs (∼60% × 2). Most of the off-chip loss is intrinsic to the symmetric DO-QKD. However, it still has some space to improve, such as the coupling ratio of the fiber couplers and the efficiencies of SNSPDs. Hence, a secure key rate of several tens of bit/s could be expected in a reconfigurable QKD network supported by a modified setup with the same silicon quantum photonic chip design.

Another important reason for the low secure key rates is the impact of the network topology. The PBSUs based on beam splitters are designed on the chip to extend the users in the QKD network, introducing an additional loss of 18 dB on each

link. If a network with fewer users is considered by reducing the number of users in each subnet, the secure key rates could be improved significantly since the same entanglement resources would be shared by fewer users.

B. Scalability of the PR-EDN

The scalability of the proposed PR-EDN scheme is based on the advantages of silicon quantum photonics. Multiple quantum light sources could be designed and fabricated on the silicon chip, providing rich quantum entanglement resources to support a large-scale EDN. Moreover, large arrays of on-chip interferometers, beam splitters, and optical switches could also be designed and fabricated on the same chip, supporting rich functions of quantum state manipulation and distribution.

In this work, the proposed PR-EDN is an SDM network. The entanglement distribution between different subnets is based on the BSGUs. One BSGU can create an entanglement link between two subnets. Therefore, n subnets need $n(n-1)/2$ BSGUs for the fully connected EDN. Thanks to the high-density photonic integration of silicon quantum photonics, it can be expected that a sufficiently large array of BSGUs could be realized on a chip to support a network with many subnets and complicated network topology. These BSGUs are parallel. No additional loss would be introduced if more BSGUs are fabricated on the chip. Moreover, each subnet would receive photons from different BSGUs, which supports the connections between different subnets. An array of beam splitters and/or optical switches is required to combine these photons and send them to different users. Its scale is determined by the number of subnets and the user number in each subnet. In recent years, large-scale silicon photonic chips have developed rapidly, pushed by the research and development of on-chip optical systems for optical communication, optical computation, and photonic quantum computation/simulation. Especially, the port number and the stage number of cascaded MZI optical switch arrays on silicon photonic chips have been improved to several tens [56–58]. It can be expected that more subnets could be supported by the proposed scheme with the new technical progress of silicon photonics on large-scale integration. In addition, we only use two specific wavelength channels in this work. The entangled photon pairs generated by SFWM on the silicon chip have a broadband spectrum. More entanglement resources would be provided if entangled photon pairs with different wavelengths could be utilized by WDM. Introducing more wavelength channels in this scheme is also an effective way to extend the scale of the chip-based network with proper designs on handling the wavelength and path degrees of freedom simultaneously.

4. CONCLUSION

In summary, a PR-EDN is proposed in this work, in which the entanglement resources are generated and distributed by a silicon quantum photonic chip. On the chip, entanglement resources are generated in silicon waveguides by SFWM and distributed to users by controllable quantum interference and passive beam splitting. A chip sample is designed and fabricated, supporting a PR-EDN with 3 subnets and 24 users. By controlling the TOPSs on the chip, the topology of the PR-EDN could be reconfigured at the intra-subnet state, inter-subnet state, and all-subnet state. It is demonstrated experimentally by measuring the entanglement distribution of all the 15 links among 6 representative users. Furthermore, a reconfigurable entanglement-based QKD network is realized as an application of the PR-EDN. The experimental results show that silicon quantum photonic chips have great potential for realizing large-scale PR-EDN, thanks to their capacities on generating and manipulating plenty of entanglement resources.

APPENDIX A: METHOD FOR CONTROLLING THE NETWORK TOPOLOGY

The reconfigurable entanglement distribution is realized by adjusting the TOPSs in BSGUs. The output state $|\Psi_2\rangle$ of one BSGU is determined by the relative phase ϕ, as shown in Eq. (2). In the experiments, we adjust ϕ by applying different voltages on TOPSs and record the coincidence counts between users in different subnets to determine the voltages for the three network states. A representative result of one of the three BSGUs under increasing voltage on the TOPS is shown in Fig. 5. It can be seen that the coincidence counts vary sinusoidally with the square of the voltages. The relative phase in MZIs will change π when the square of the voltage changes about 15 V^2, which results in a 2π change in the sinusoidal fringe of coincidence counts. The coincidence counts reach a maximum at the voltage indicated by the red arrow, corresponding to $|\Psi_{split}\rangle$. It is the voltage supporting the inter-subnet state in this BSGU, whereas the coincidence counts reach a minimum at the voltage indicated by the blue arrow, corresponding to $|\Psi_{bunch}\rangle$. It is the voltage supporting the intra-subnet state in this BSGU. To realize a superposition of $|\Psi_{split}\rangle$ and $|\Psi_{bunch}\rangle$, the voltage should be adjusted to the value indicated by the yellow arrow, which supports the all-subnet state. The voltages of the TOPSs in the three BSGUs for the different

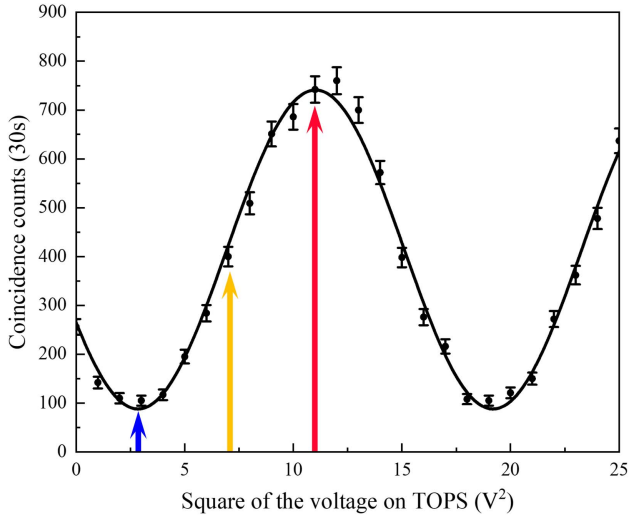

Fig. 5. Coincidence counts of two users in different subnets under increasing TOPS voltage in the corresponding BSGU. The voltages indicated by the blue, red, and yellow arrows represent the values supporting the intra-subnet state, inter-subnet state, and all-subnet state, respectively. Error bars come from the Poisson distribution of photons.

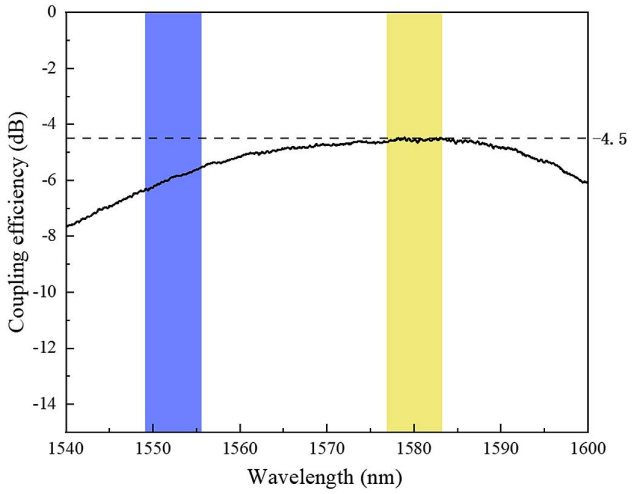

Fig. 6. Coupling efficiency between the on-chip grating couplers and optical fibers. The blue region is the wavelength range of photon pair generation. The yellow region is the wavelength range with the highest coupling efficiency, which is ~ – 4.5 dB.

network states are determined independently by this method. In the experiments, all the voltages are below 7 V.

APPENDIX B: FABRICATION PROCESS AND COUPLING EFFICIENCY OF THE CHIP

The PR-EDN chip is fabricated on an SOI substrate with a 220 nm top-silicon layer. The ZEP-520A photoresist is first spined on the substrate and followed by the electron beam lithography (EBL) to define patterns of all the silicon devices. Then, the patterns are transferred to the top-silicon layer by the inductively coupled plasma (ICP) dry etching processes. The etching depths are 70 nm for grating couplers and 220 nm for other silicon devices. A 1-μm-thick silica layer is deposited by plasma-enhanced chemical vapor deposition (PECVD) on the etched silicon devices, which is used as a protected layer. Finally, metallization processes, consisting of an ultraviolet lithography process followed by electron beam evaporation and a lift-off process, are used to form the 100 nm titanium heaters in TOPSs. Other conducting wires and pads are formed

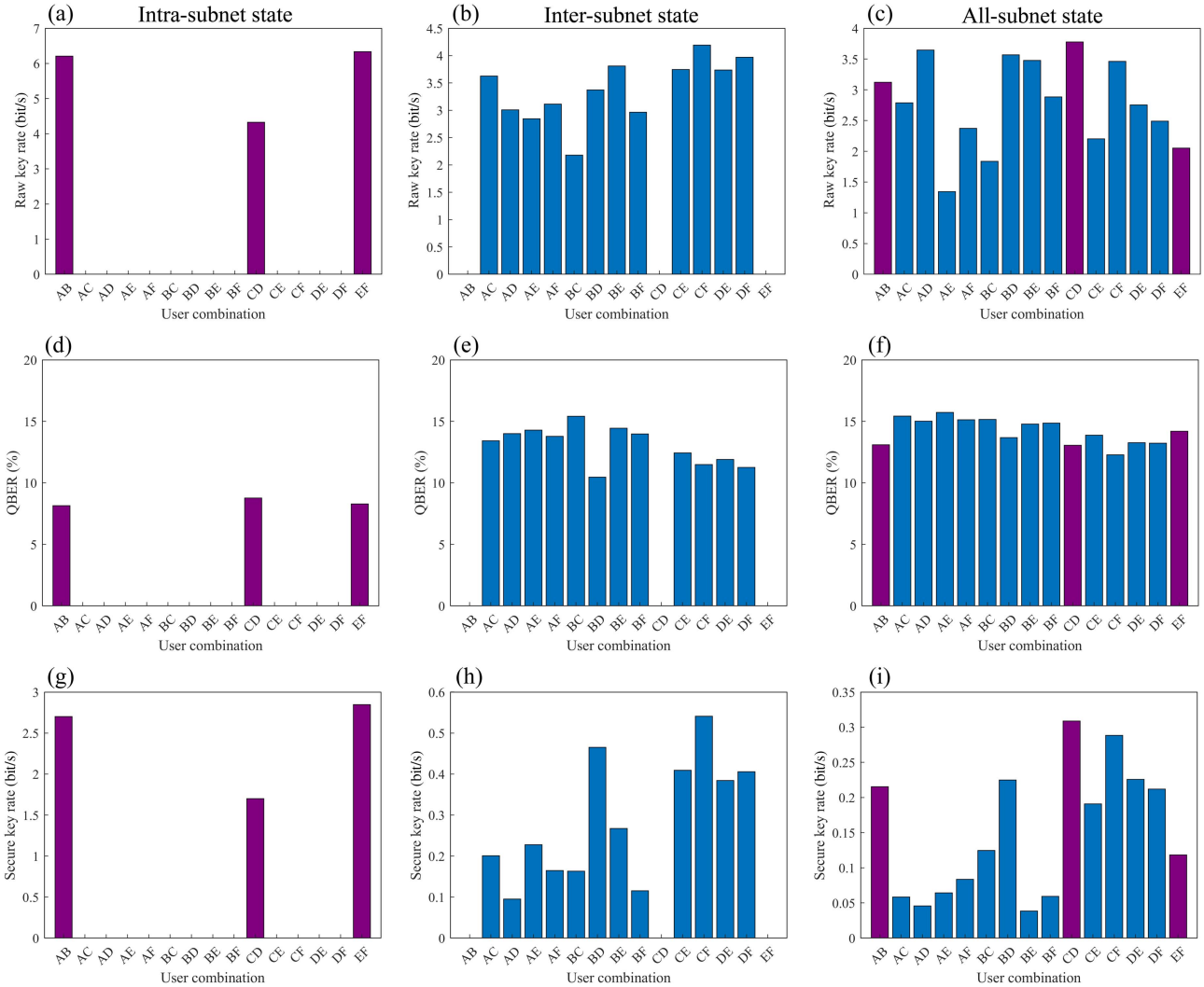

Fig. 7. Detail performance of the reconfigurable QKD network. (a)–(c) Measured raw key rates, (d)–(f) QBERs, and (g)–(i) secure key rates in finite-size regime at the intra-subnet state, inter-subnet state, and all-subnet state, respectively.

by 300 nm aluminum. The core area of the PR-EDN chip, shown in Fig. 1(b), is 3.1 mm × 0.7 mm.

The geometry of waveguides used as nonlinear media in BSGUs is 450 nm × 220 nm with a propagation loss of ∼0.5 dB/mm. To improve the performance of entanglement distribution, straight waveguides with a width of 1.2 μm are applied in the photonic circuits except for BSGUs, which can reduce the scattering loss due to the roughness of waveguide sidewalls. In the bend section, the width of waveguides is still 450 nm, preventing the impact of higher-order modes. Two adiabatic tapers with a length of 100 μm are used as the transition area between the waveguides with different widths.

Figure 6 shows the measured coupling efficiency between on-chip grating couplers and optical fibers. Due to the deviation in the fabrication, the highest coupling efficiency appears near 1580 nm (the yellow region in Fig. 6), which is ∼ − 4.5 dB. However, the coupling efficiency at the wavelength of signal and idler photons (blue region in Fig. 6) is ∼ − 6 dB. It can be expected that the coupling efficiency of the chip could be significantly improved by state-of-the-art coupling methods [53–55].

APPENDIX C: DETAIL PERFORMANCE OF THE RECONFIGURABLE QKD NETWORK BASED ON SYMMETRIC DO-QKD

In our previous works, the details of the key generation and security test in symmetric DO-QKD have been discussed

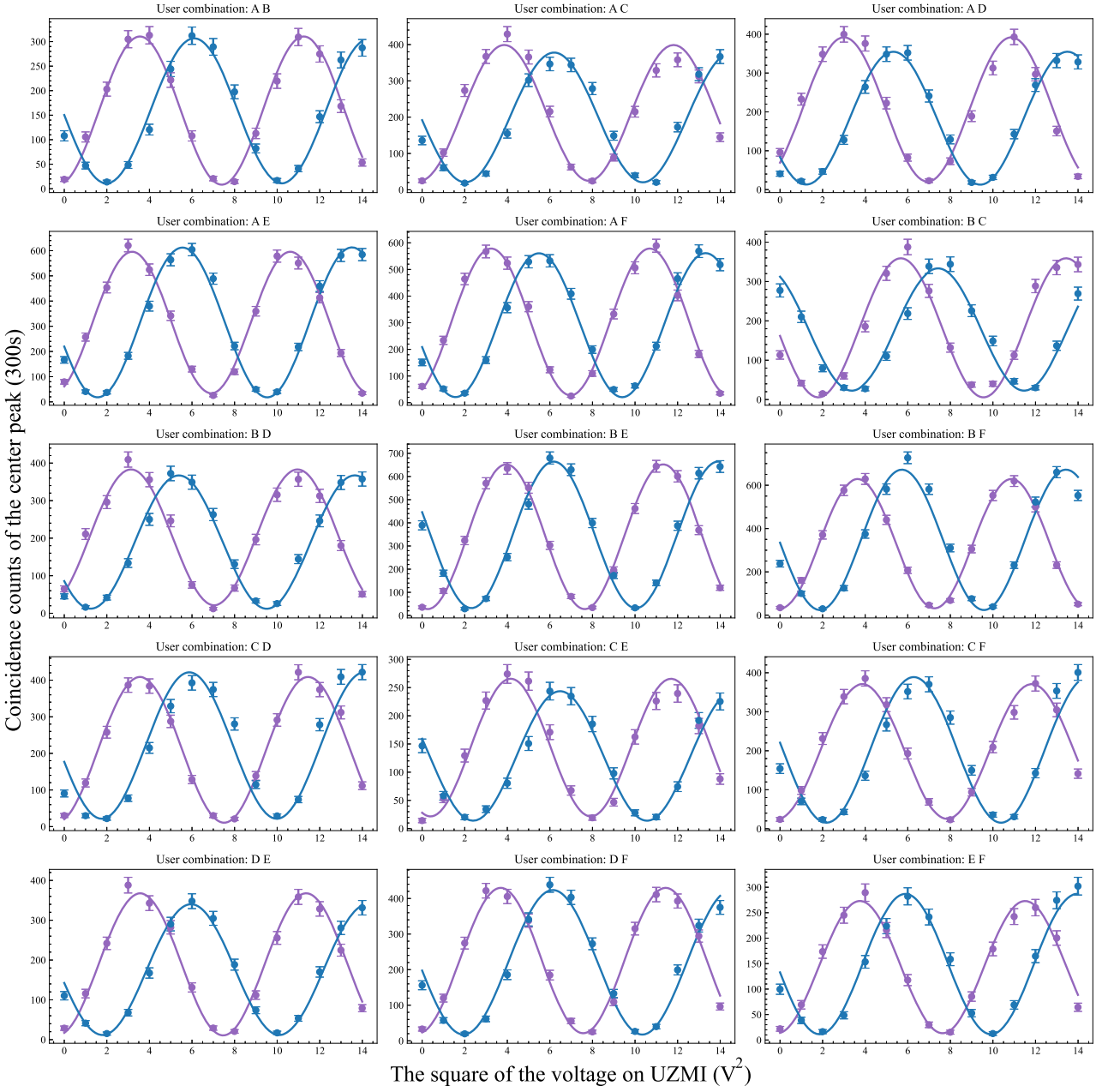

Fig. 8. Experimental results of the Franson type interference on all the links among the six representative users (users A–F).

[26,30,59]. Secure keys can be obtained from the arrival time of the energy-time entangled photon pairs by high-dimensional time encoding. First, we assume that in a period of time, named a "frame," the average number of arrival photons is far less than 1. Then, we divide one frame into four slots labeled as "00," "01," "10," and "11," and there are three bins in one slot. Two users compare the frame numbers and bin numbers of the single-photon events they recorded. If two single-photon events at the two sides have the same frame number and bin number, they are selected out as a coincidence event. The raw keys can be obtained from the slot labels of the coincidence events at the two sides.

The security of symmetric DO-QKD is guaranteed by the nonlocal dispersion cancellation effect [60], which is accomplished by a normal dispersion component and an anomalous dispersion component in the QKD user end, as shown in the inset figure of Fig. 2(c). The joint measurements of the time-frequency covariance matrix can be performed by the data obtained by four SNSPDs in two different users, from which we can calculate the secure key capacity. Details of calculating the secure key capacity can be found in Refs. [26,30,52,59]. The secure key rates shown in Fig. 3 can be obtained from raw key rates and the secure key capacity.

In our experiments, the count rate for all the users is several tens of kHz, ensuring the sparsity of arrival photons in one frame (several nanoseconds). To evaluate the impact of the finite-size effect [61], we continuously take the measurement for 3 h at the network link where the two users share entanglement resources (for example, users A and B in the intra-subnet state) and for 1 h at the network link where the two users do not share entanglement resource (for example, users A and C in the intra-subnet state). The bin widths used in the intra-subnet state, inter-subnet state, and all-subnet state are 300 ps, 150 ps, and 100 ps, respectively, which have been optimized for a high raw key rate with low QBER. The results of raw key rates and QBER are shown in Figs. 7(a)–7(f). It can be seen that raw keys could not be generated with a reasonable QBER for the two users sharing no entanglement resource. In addition, all the links with available entanglement resources obtained secure keys in the finite-size regime, as shown in Figs. 7(g)–7(i). The methods to improve the performance of DO-QKD have been discussed in the main manuscript.

APPENDIX D: EXPERIMENTAL RESULTS OF THE FRANSON-TYPE INTERFERENCE

To verify the property of energy-time entanglement of the photon pairs distributed by the PR-EDN chip, we perform the Franson-type interference by two UMZIs on all the 15 links among the six representative users (users A–F). In each measurement, we fix the phase α of one UMZI at θ and $\theta + \pi/2$, and sweep the phase β of another UMZI, respectively. The path difference between two arms in the UMZI (Kylia Inc.) is 400 ps. At each setting of UMZIs, time-resolved coincidence counts are measured for 300 s, and the counts of the center coincidence peak are recorded in a time window of 64 ps. Figure 8 shows all the experimental results of the 15 links. The blue and purple points are the experimental data measured under $\alpha = \theta$ and $\alpha = \theta + \pi/2$, respectively, and the blue and purple lines are their fitting curves. Since the phase differences of the UMZIs are proportional to squares of the voltages applied on the heaters of the two UMZI, β is represented by the squares of the voltages on the corresponding UMZIs. It can be seen that sinusoidal interference fringes under two mutually unbiased bases can be obtained clearly in the experiments of all the links. The raw (without subtracting accidental coincidence counts) and the net (with subtracting accidental coincidence counts) visibilities of two-photon interference fringes in Fig. 8 are shown in Table 1. It can be seen that most fringes have a net visibility higher than 90%. The average net visibilities of under two mutually unbiased bases are 91.8% ± 2.0% and 94.6% ± 1.9%, respectively. The lowest net visibility appears at link CE with a value of 87.9%, which is far higher than $1/\sqrt{2}$ (70.7%). These results indicate that the energy-time entanglement is distributed to different users by the PR-EDN chip successfully.

Table 1. Raw and Net Visibility of Two-Photon Interference Fringes

	$\alpha = \theta$		$\alpha = \theta + \pi/2$	
User Combination	Raw	Net	Raw	Net
AB	94.8% ± 2.1%	97.2% ± 2.2%	93.1% ± 3.6%	95.6% ± 3.7%
AC	88.3% ± 3.4%	91.3% ± 3.6%	89.7% ± 4.3%	92.7% ± 4.5%
AD	90.0% ± 3.5%	93.4% ± 3.7%	93.1% ± 2.7%	96.7% ± 2.9%
AE	89.2% ± 1.7%	91.8% ± 1.8%	94.3% ± 2.3%	96.9% ± 2.4%
AF	91.0% ± 1.8%	93.4% ± 1.8%	92.9% ± 2.3%	95.4% ± 2.5%
BC	96.9% ± 3.7%	100.0% ± 4.0%	87.3% ± 3.5%	91.6% ± 3.9%
BD	89.5% ± 2.7%	92.8% ± 2.9%	93.7% ± 2.6%	97.2% ± 2.7%
BE	91.9% ± 1.2%	94.4% ± 1.3%	90.9% ± 2.5%	93.5% ± 2.6%
BF	90.4% ± 1.1%	92.7% ± 1.2%	93.1% ± 3.9%	95.6% ± 4.1%
CD	94.9% ± 2.1%	96.3% ± 2.1%	90.3% ± 5.5%	91.4% ± 5.6%
CE	84.9% ± 3.1%	87.8% ± 3.3%	89.1% ± 2.9%	92.7% ± 3.1%
CF	87.2% ± 2.2%	89.9% ± 2.3%	92.3% ± 5.1%	95.0% ± 5.4%
DE	94.3% ± 2.6%	97.1% ± 2.7%	93.4% ± 2.2%	96.1% ± 2.3%
DF	90.6% ± 2.3%	93.2% ± 2.4%	92.1% ± 3.1%	94.9% ± 3.3%
EF	90.7% ± 2.2%	92.0% ± 2.3%	92.4% ± 3.1%	93.7% ± 3.2%

Funding. National Key Research and Development Program of China (2018YFB2200400); Beijing Municipal Natural Science Foundation (Z180012); National Natural Science Foundation of China (61875101, 91750206); Tsinghua Initiative Scientific Research Program.

Disclosures. The authors declare no conflicts of interest.

Data Availability. Data underlying the results presented in this paper are not publicly available at this time but may be obtained from the authors upon reasonable request.

REFERENCES

1. S. Wehner, D. Elkouss, and R. Hanson, "Quantum internet: a vision for the road ahead," Science **362**, eaam9288 (2018).
2. S.-H. Wei, B. Jing, X.-Y. Zhang, J.-Y. Liao, C.-Z. Yuan, B.-Y. Fan, C. Lyu, D.-L. Zhou, Y. Wang, G.-W. Deng, H.-Z. Song, D. Oblak, G.-C. Guo, and Q. Zhou, "Towards real-world quantum networks: a review," Laser Photon. Rev. **16**, 2100219 (2022).
3. T. Inagaki, N. Matsuda, O. Tadanaga, M. Asobe, and H. Takesue, "Entanglement distribution over 300 km of fiber," Opt. Express **21**, 23241–23249 (2013).
4. A. Fedrizzi, R. Ursin, T. Herbst, M. Nespoli, R. Prevedel, T. Scheidl, F. Tiefenbacher, T. Jennewein, and A. Zeilinger, "High-fidelity transmission of entanglement over a high-loss free-space channel," Nat. Phys. **5**, 389–392 (2009).
5. J. Yin, Y. Cao, Y.-H. Li, S.-K. Liao, L. Zhang, J.-G. Ren, W.-Q. Cai, W.-Y. Liu, B. Li, H. Dai, G.-B. Li, Q.-M. Lu, Y.-H. Gong, Y. Xu, S.-L. Li, F.-Z. Li, Y.-Y. Yin, Z.-Q. Jiang, M. Li, J.-J. Jia, G. Ren, D. He, Y.-L. Zhou, X.-X. Zhang, N. Wang, X. Chang, Z.-C. Zhu, N.-L. Liu, Y.-A. Chen, C.-Y. Lu, R. Shu, C.-Z. Peng, J.-Y. Wang, and J.-W. Pan, "Satellite-based entanglement distribution over 1200 kilometers," Science **356**, 1140–1144 (2017).
6. T. Lutz, P. Kolenderski, and T. Jennewein, "Toward a downconversion source of positively spectrally correlated and decorrelated telecom photon pairs," Opt. Lett. **38**, 697–699 (2013).
7. T. Kim, M. Fiorentino, and F. N. Wong, "Phase-stable source of polarization-entangled photons using a polarization Sagnac interferometer," Phys. Rev. A **73**, 012316 (2006).
8. Z. Zhang, C. Yuan, S. Shen, H. Yu, R. Zhang, H. Wang, H. Li, Y. Wang, G. Deng, Z. Wang, L. You, Z. Wang, H. Song, G. Guo, and Q. Zhou, "High-performance quantum entanglement generation via cascaded second-order nonlinear processes," npj Quantum Inf. **7**, 123 (2021).
9. J. Zhao, C. Ma, M. Rüsing, and S. Mookherjea, "High quality entangled photon pair generation in periodically poled thin-film lithium niobate waveguides," Phys. Rev. Lett. **124**, 163603 (2020).
10. U. A. Javid, J. Ling, J. Staffa, M. Li, Y. He, and Q. Lin, "Ultrabroadband entangled photons on a nanophotonic chip," Phys. Rev. Lett. **127**, 183601 (2021).
11. G.-T. Xue, Y.-F. Niu, X. Liu, J.-C. Duan, W. Chen, Y. Pan, K. Jia, X. Wang, H.-Y. Liu, Y. Zhang, P. Xu, G. Zhao, X. Cai, Y.-X. Gong, X. Hu, Z. Xie, and S. Zhu, "Ultrabright multiplexed energy-time-entangled photon generation from lithium niobate on insulator chip," Phys. Rev. Appl. **15**, 064059 (2021).
12. N. A. Lange, J. P. Höpker, R. Ricken, V. Quiring, C. Eigner, C. Silberhorn, and T. J. Bartley, "Cryogenic integrated spontaneous parametric down-conversion," Optica **9**, 108–111 (2022).
13. H. Yu, C. Yuan, R. Zhang, Z. Zhang, H. Li, Y. Wang, G. Deng, L. You, H. Song, Z. Wang, G.-C. Guo, and Q. Zhou, "Spectrally multiplexed indistinguishable single-photon generation at telecom-band," Photon. Res. **10**, 1417–1429 (2022).
14. J. Chen, K. F. Lee, and P. Kumar, "Deterministic quantum splitter based on time-reversed Hong-Ou-Mandel interference," Phys. Rev. A **76**, 031804 (2007).
15. S. D. Dyer, B. Baek, and S. W. Nam, "High-brightness, low-noise, all-fiber photon pair source," Opt. Express **17**, 10290–10297 (2009).
16. X. Li, L. Yang, X. Ma, L. Cui, Z. Y. Ou, and D. Yu, "All-fiber source of frequency-entangled photon pairs," Phys. Rev. A **79**, 033817 (2009).
17. Q. Zhou, S. Dong, W. Zhang, L. You, Y. He, W. Zhang, Y. Huang, and J. Peng, "Frequency-entanglement preparation based on the coherent manipulation of frequency nondegenerate energy-time entangled state," J. Opt. Soc. Am. B **31**, 1801–1806 (2014).
18. K.-I. Harada, H. Takesue, H. Fukuda, T. Tsuchizawa, T. Watanabe, K. Yamada, Y. Tokura, and S.-I. Itabashi, "Frequency and polarization characteristics of correlated photon-pair generation using a silicon wire waveguide," IEEE J. Sel. Top. Quantum Electron. **16**, 325–331 (2009).
19. N. Matsuda, H. Le Jeannic, H. Fukuda, T. Tsuchizawa, W. J. Munro, K. Shimizu, K. Yamada, Y. Tokura, and H. Takesue, "A monolithically integrated polarization entangled photon pair source on a silicon chip," Sci. Rep. **2**, 817 (2012).
20. L. Olislager, J. Safioui, S. Clemmen, K. P. Huy, W. Bogaerts, R. Baets, P. Emplit, and S. Massar, "Silicon-on-insulator integrated source of polarization-entangled photons," Opt. Lett. **38**, 1960–1962 (2013).
21. J. W. Silverstone, D. Bonneau, K. Ohira, N. Suzuki, H. Yoshida, N. Iizuka, M. Ezaki, C. M. Natarajan, M. G. Tanner, R. H. Hadfield, V. Zwiller, G. D. Marshall, J. G. Rarity, J. L. O'Brien, and M. G. Thompson, "On-chip quantum interference between silicon photon-pair sources," Nat. Photonics **8**, 104–108 (2014).
22. A. Ciurana, V. Martin, J. Martinez-Mateo, B. Schrenk, M. Peev, and A. Poppe, "Entanglement distribution in optical networks," IEEE J. Sel. Top. Quantum Electron. **21**, 37–48 (2014).
23. S. Wengerowsky, S. K. Joshi, F. Steinlechner, H. Hübel, and R. Ursin, "An entanglement-based wavelength-multiplexed quantum communication network," Nature **564**, 225–228 (2018).
24. F. Appas, F. Baboux, M. I. Amanti, A. Lematre, F. Boitier, E. Diamanti, and S. Ducci, "Flexible entanglement-distribution network with an AlGaAs chip for secure communications," npj Quantum Inf. **7**, 118 (2021).
25. N. B. Lingaraju, H.-H. Lu, S. Seshadri, D. E. Leaird, A. M. Weiner, and J. M. Lukens, "Adaptive bandwidth management for entanglement distribution in quantum networks," Optica **8**, 329–332 (2021).
26. X. Liu, X. Yao, R. Xue, H. Wang, H. Li, Z. Wang, L. You, X. Feng, F. Liu, K. Cui, Y. Huang, and W. Zhang, "An entanglement-based quantum network based on symmetric dispersive optics quantum key distribution," APL Photon. **5**, 076104 (2020).
27. S. K. Joshi, D. Aktas, S. Wengerowsky, M. Lončarić, S. P. Neumann, B. Liu, T. Scheidl, G. C. Lorenzo, Ž. Samec, L. Kling, A. Qiu, M. Razavi, M. Stipcevic, J. G. Rarity, and R. Ursin, "A trusted node-free eight-user metropolitan quantum communication network," Sci. Adv. **6**, eaba0959 (2020).
28. M. Alshowkan, B. P. Williams, P. G. Evans, N. S. Rao, E. M. Simmerman, H.-H. Lu, N. B. Lingaraju, A. M. Weiner, C. E. Marvinney, Y.-Y. Pai, B. J. Lawrie, N. A. Peters, and J. M. Lukens, "Reconfigurable quantum local area network over deployed fiber," PRX Quantum **2**, 040304 (2021).
29. J.-H. Kim, J.-W. Chae, Y.-C. Jeong, and Y.-H. Kim, "Quantum communication with time-bin entanglement over a wavelength-multiplexed fiber network," APL Photon. **7**, 016106 (2022).
30. X. Liu, J. Liu, R. Xue, H. Wang, H. Li, X. Feng, F. Liu, K. Cui, Z. Wang, L. You, Y. Huang, and W. Zhang, "40-user fully connected entanglement-based quantum key distribution network without trusted node," PhotoniX **3**, 2 (2022).
31. E. Fitzke, L. Bialowons, T. Dolejsky, M. Tippmann, O. Nikiforov, T. Walther, F. Wissel, and M. Gunkel, "Scalable network for simultaneous pairwise quantum key distribution via entanglement-based time-bin coding," PRX Quantum **3**, 020341 (2022).
32. Z. Huang, S. K. Joshi, D. Aktas, C. Lupo, A. O. Quintavalle, N. Venkatachalam, S. Wengerowsky, M. Lončarić, S. P. Neumann, B. Liu, Ž. Samec, L. Kling, M. Stipčević, R. Ursin, and J. G. Rarity, "Experimental implementation of secure anonymous protocols on an eight-user quantum key distribution network," npj Quantum Inf. **8**, 25 (2022).
33. S. Paesani, M. Borghi, S. Signorini, A. Manos, L. Pavesi, and A. Laing, "Near-ideal spontaneous photon sources in silicon quantum photonics," Nat. Commun. **11**, 2505 (2020).

34. L. Lu, L. Xia, Z. Chen, L. Chen, T. Yu, T. Tao, W. Ma, Y. Pan, X. Cai, Y. Lu, S. Zhu, and X.-S. Ma, "Three-dimensional entanglement on a silicon chip," npj Quantum Inf. **6**, 30 (2020).
35. D.-N. Liu, J.-Y. Zheng, L.-J. Yu, X. Feng, F. Liu, K.-Y. Cui, Y.-D. Huang, and W. Zhang, "Generation and dynamic manipulation of frequency degenerate polarization entangled bell states by a silicon quantum photonic circuit," Chip **1**, 100001 (2022).
36. T. Dai, Y. Ao, J. Bao, J. Mao, Y. Chi, Z. Fu, Y. You, X. Chen, C. Zhai, B. Tang, Y. Yang, Z. Li, L. Yuan, F. Gao, X. Lin, M. G. Thompson, J. L. O'Brien, Y. Li, X. Hu, Q. Gong, and J. Wang, "Topologically protected quantum entanglement emitters," Nat. Photonics **16**, 248–257 (2022).
37. K. Wei, W. Li, H. Tan, Y. Li, H. Min, W.-J. Zhang, H. Li, L. You, Z. Wang, X. Jiang, T.-Y. Chen, S.-K. Liao, C.-Z. Peng, F. Xu, and J.-W. Pan, "High-speed measurement-device-independent quantum key distribution with integrated silicon photonics," Phys. Rev. X **10**, 031030 (2020).
38. L. Cao, W. Luo, Y. Wang, J. Zou, R. D. Yan, H. Cai, Y. Zhang, X. L. Hu, C. Jiang, W. J. Fan, X. Q. Zhou, B. Dong, X. S. Luo, G. Q. Lo, Y. X. Wang, Z. W. Xu, S. H. Sun, X. B. Wang, Y. L. Hao, Y. F. Jin, D. L. Kwong, L. C. Kwek, and A. Q. Liu, "Chip-based measurement-device-independent quantum key distribution using integrated silicon photonic systems," Phys. Rev. Appl. **14**, 011001 (2020).
39. H. Semenenko, P. Sibson, A. Hart, M. G. Thompson, J. G. Rarity, and C. Erven, "Chip-based measurement-device-independent quantum key distribution," Optica **7**, 238–242 (2020).
40. D. Llewellyn, Y. Ding, I. I. Faruque, S. Paesani, D. Bacco, R. Santagati, Y.-J. Qian, Y. Li, Y.-F. Xiao, M. Huber, M. Malik, G. F. Sinclair, X. Zhou, K. Rottwitt, J. L. O'Brien, J. G. Rarity, Q. Gong, L. K. Oxenlowe, J. Wang, and M. G. Thompson, "Chip-to-chip quantum teleportation and multi-photon entanglement in silicon," Nat. Phys. **16**, 148–153 (2020).
41. X. Zheng, P. Zhang, R. Ge, L. Lu, G. He, Q. Chen, F. Qu, L. Zhang, X. Cai, Y. Lu, S. Zhu, P. Wu, and X.-S. Ma, "Heterogeneously integrated, superconducting silicon-photonic platform for measurement-device-independent quantum key distribution," Adv. Photon. **3**, 055002 (2021).
42. T. K. Paraiso, T. Roger, D. G. Marangon, I. De Marco, M. Sanzaro, R. I. Woodward, J. F. Dynes, Z. Yuan, and A. J. Shields, "A photonic integrated quantum secure communication system," Nat. Photonics **15**, 850–856 (2021).
43. M. Avesani, L. Calderaro, M. Schiavon, A. Stanco, C. Agnesi, A. Santamato, M. Zahidy, A. Scriminich, G. Foletto, G. Contestabile, M. Chiesa, D. Rotta, M. Artiglia, A. Montanaro, M. Romagnoli, V. Sorianello, F. Vedovato, G. Vallone, and P. Villoresi, "Full daylight quantum-key-distribution at 1550 nm enabled by integrated silicon photonics," npj Quantum Inf. **7**, 93 (2021).
44. W. Li, L. Zhang, H. Tan, Y. Lu, S.-K. Liao, J. Huang, H. Li, Z. Wang, H.-K. Mao, B. Yan, Q. Li, Y. Liu, Q. Zhang, C.-Z. Peng, L. You, F. Xu, and J.-W. Pan, "High-rate quantum key distribution exceeding 110 Mb s^{-1}," Nat. Photonics **17**, 416–421 (2023).
45. X. Qiang, Y. Wang, S. Xue, R. Ge, L. Chen, Y. Liu, A. Huang, X. Fu, P. Xu, T. Yi, F. Xu, M. Deng, J. B. Wang, J. D. A. Meinecke, J. C. F. Matthews, X. Cai, X. Yang, and J. Wu, "Implementing graph-theoretic quantum algorithms on a silicon photonic quantum walk processor," Sci. Adv. **7**, eabb8375 (2021).
46. C. Vigliar, S. Paesani, Y. Ding, J. C. Adcock, J. Wang, S. Morley-Short, D. Bacco, L. K. Oxenløwe, M. G. Thompson, J. G. Rarity, and A. Laing, "Error-protected qubits in a silicon photonic chip," Nat. Phys. **17**, 1137–1143 (2021).
47. Y. Chi, J. Huang, Z. Zhang, J. Mao, Z. Zhou, X. Chen, C. Zhai, J. Bao, T. Dai, H. Yuan, M. Zhang, D. Dai, B. Tang, Y. Yang, Z. Li, Y. Ding, L. K. Oxenløwe, M. G. Thompson, J. L. O'Brien, Y. Li, Q. Gong, and J. Wang, "A programmable qudit-based quantum processor," Nat. Commun. **13**, 1166 (2022).
48. J. Bao, Z. Fu, T. Pramanik, J. Mao, Y. Chi, Y. Cao, C. Zhai, Y. Mao, T. Dai, X. Chen, X. Jia, L. Zhao, Y. Zheng, B. Tang, Z. Li, J. Luo, W. Wang, Y. Yang, Y. Peng, D. Liu, D. Dai, Q. He, A. L. Muthali, L. K. Oxenløwe, C. Vigliar, S. Paesani, H. Hou, R. Santagati, J. W. Silverstone, A. Laing, M. G. Thompson, J. L. O'Brien, Y. Ding, Q. Gong, and J. Wang, "Very-large-scale integrated quantum graph photonics," Nat. Photonics, https://doi.org/10.1038/s41566-023-01187-z (2023).
49. J. D. Franson, "Bell inequality for position and time," Phys. Rev. Lett. **62**, 2205–2208 (1989).
50. P. G. Kwiat, A. M. Steinberg, and R. Y. Chiao, "High-visibility interference in a Bell-inequality experiment for energy and time," Phys. Rev. A **47**, R2472–R2475 (1993).
51. W. Tittel, J. Brendel, N. Gisin, and H. Zbinden, "Long-distance Bell-type tests using energy-time entangled photons," Phys. Rev. A **59**, 4150–4163 (1999).
52. C. Lee, Z. Zhang, G. R. Steinbrecher, H. Zhou, J. Mower, T. Zhong, L. Wang, X. Hu, R. D. Horansky, V. B. Verma, A. E. Lita, R. P. Mirin, F. Marsili, M. D. Shaw, S. W. Nam, G. W. Wornell, F. N. C. Wong, J. H. Shapiro, and D. Englund, "Entanglement-based quantum communication secured by nonlocal dispersion cancellation," Phys. Rev. A **90**, 062331 (2014).
53. Y. Ding, C. Peucheret, H. Ou, and K. Yvind, "Fully etched apodized grating coupler on the SOI platform with –0.58 dB coupling efficiency," Opt. Lett. **39**, 5348–5350 (2014).
54. R. Marchetti, C. Lacava, L. Carroll, K. Gradkowski, and P. Minzioni, "Coupling strategies for silicon photonics integrated chips," Photon. Res. **7**, 201–239 (2019).
55. W. Zhang, M. Ebert, J. D. Reynolds, B. Chen, X. Yan, H. Du, M. Banakar, D. T. Tran, C. G. Littlejohns, G. T. Reed, and D. J. Thomson, "Buried 3D spot-size converters for silicon photonics," Optica **8**, 1102–1108 (2021).
56. L. Qiao, W. Tang, and T. Chu, "32 × 32 silicon electro-optic switch with built-in monitors and balanced-status units," Sci. Rep. **7**, 42306 (2017).
57. P. Dumais, D. J. Goodwill, D. Celo, J. Jiang, C. Zhang, F. Zhao, X. Tu, C. Zhang, S. Yan, J. He, M. Li, W. Liu, Y. Wei, D. Geng, H. Mehrvar, and E. Bernier, "Silicon photonic switch subsystem with 900 monolithically integrated calibration photodiodes and 64-fiber package," J. Lightwave Technol. **36**, 233–238 (2017).
58. K. Suzuki, R. Konoike, J. Hasegawa, S. Suda, H. Matsuura, K. Ikeda, S. Namiki, and H. Kawashima, "Low-insertion-loss and power-efficient 32 × 32 silicon photonics switch with extremely high-Δ silica PLC connector," J. Lightwave Technol. **37**, 116–122 (2018).
59. X. Liu, X. Yao, H. Wang, H. Li, Z. Wang, L. You, Y. Huang, and W. Zhang, "Energy-time entanglement-based dispersive optics quantum key distribution over optical fibers of 20 km," Appl. Phys. Lett. **114**, 141104 (2019).
60. J. Franson, "Nonlocal cancellation of dispersion," Phys. Rev. A **45**, 3126–3132 (1992).
61. C. Lee, J. Mower, Z. Zhang, J. H. Shapiro, and D. Englund, "Finite-key analysis of high-dimensional time–energy entanglement-based quantum key distribution," Quantum Inf. Process. **14**, 1005–1015 (2015).